The final publication is available at

https://doi.org/10.1016/j.enconman.2021.113888

Additional Information

Influence of the cell geometry on the conversion efficiency of oxidation catalysts under real driving conditions

Pedro Piqueras[a,*], María José Ruiz[a], José Martín Herreros[b], Athanasios Tsolakis[b]

[a]*CMT-Motores Térmicos, Universitat Politècnica de València, Camino de Vera s/n, 46022 Valencia, Spain.*
[b]*Deparment of Mechanical Engineering, University of Birmingham, Edgbaston B15 2TT, UK.*

Abstract

Worldwide pollutant regulations applied to the transportation sector are progressively tightening the emission limits and widening the operating conditions of the type approval tests. As a result, the layout and thermal management of the exhaust system is becoming highly complex looking to achieve early catalytic converter activation. On this regard, the monolith meso-geometry plays a primary role to optimise the pollutants conversion efficiency. The geometrical characteristics simultaneously affect and trade-off multiple flow phenomena as the exhaust gas is transported through the channels. These include the bulk gas and internal pore diffusion towards the active sites in addition to the heat transfer including convection, radial conductivity and thermal capacitance. In this work, the impacts of the cell size, cross-section shape, washcoat loading and substrate material on CO and HC conversion efficiency have been investigated under representative real driving conditions. From the real driving conditions experimental data, the study decouples the influence of the washcoat loading from the cell size and material applying a catalytic converter model. Detailed expressions are provided for the calculation of the specific surfaces and heat and mass transfer parameters as a function of the cell and washcoat meso-geometry in square and triangular cells. Therefore, this work enables to identify the processes which govern the catalytic abatement of pollutant emissions. In particular, the role of the gas and washcoat specific surfaces is highlighted because of its importance on the optimization of the mass transfer process by means of a proper cell geometry selection. In parallel, the differences in the change of the CO and HC abatement patterns, which are explained by the characteristic CO emission spikes in accelerations and the HC accumulation, contribute to evidence the limitations on the conversion efficiency benefit that the optimum cell geometry and washcoat loading can provide.

1

1. Introduction

Current and future emissions standards are pursuing zero local pollutant emissions. Therefore, the elements involved in the emissions control, from the source to the final stage of abatement in the aftertreatment system, need to be revisited to make them efficient contributors to the pollutants abatement under the new boundaries [1]. In particular, the aftertreatment systems have become standard and embedded both in compression and spark ignition engines to reduce the tailpipe pollutant emissions [2]. In this context, improving the aftertreatment performance by means of optimised catalyst formulation [3], impregnation and carrier [4] for faster light-off is not effectively enough [5] to fulfil incoming emissions regulations applied to real driving conditions [6]. The complexity of emission reduction under realistic transient conditions demands the conjoint design of exhaust systems and thermal management strategies, what actively involves the combustion process [7], turbocharger [8] and advanced exhaust components. Such a scenario demands a comprehensive and precise understanding of the processes governing the pollutants depletion by means of experimental [9] and modelling tools [10].

With this approach, the monolith design can bring relevant improvements to the conversion efficiency, as required by new combustion concepts [11]. It can be promoted by means of modifications of the monolith physical properties, adapting the substrate [12] or cell size [13] to the flow properties, considering the washcoat loading effect on the cross-section geometry [14] or attending to the porous substrate properties [15]. The arrangement of the channels has a primary potential to alter the conversion efficiency [16]. It is possible to increase the exhaust gas to catalytic area by increasing the cell density and enhance the heat and mass transfer in the channels by reducing the cell hydraulic diameter [17]. Combined with the use of thinner walls also minimises the substrate mass so that the warm-up is accelerated [18] and can provide benefits in inertial pressure drop

---

*Corresponding author. Tel.: +34 96 3877650, fax: +34 96 3877659.
Email address: pedpicab@mot.upv.es (Pedro Piqueras)

contributions [19]. However, if the channel walls become too thin, they become extremely fragile and eventually break. An alternative solution is the use of triangular or wave channels to improve the thermal strength [20]. In that sense, metallic substrates with triangular cells [21] allow the use of higher cell densities, whilst maintaining mechanical strength and thermal durability. However, this is done so at the expense of higher thermal conductivity. In addition, some concerns have been raised about washcoat adhesion on metallic walls [22] due to the reduced roughness of the non-porous surface and the differences in thermal expansion between substrate and washcoat. From a cost point of view, these substrates are also more expensive on average than their ceramic counterparts.

This study investigates the potential of varying cell geometries and substrates to enhance pollutant conversion efficiency under real driving conditions represented by the Worldwide harmonized Light vehicles Test Cycle (WLTC). A commercial cordierite oxidation catalyst with square cells was taken as baseline design. This selection simplifies the discussion on the chemical mechanism to put the focus on the geometry effects while considering the different fashion in raw pollutant emissions under highly dynamic operation. This way, the characteristic CO emission spikes during accelerations and the HC accumulation capability are identified as phenomena determining the trends in cell geometry and washcoat loading optimization at the same time that involve limitations to the expected benefits in conversion efficiency. For this discussion, a catalytic converter model for flow-through monoliths [23] solving heat transfer and chemical species transport was used. Its use provided flexibility to adapt the numerical solver to square and triangular cells with accurate control on the boundary conditions. The model formulation is described with special detail in explicit expressions for outlet pollutants mole fraction calculation and the definition of the specific surfaces and heat and mass transfer parameters. Their expressions are provided for square and triangular cell cross-sections including the sensitivity to the washcoat loading. This theoretical background supports the discussion on the role of the geometric parameters on the mass and heat transfer, which then govern the pollutant conversion efficiency. In particular, variations in cell shape and density, washcoat loading and substrate material were simulated. The contributions of the involved abatement mechanisms were also evaluated considering their sensitivity to the ex-

3

haust flow properties. As a result, the application of the model provides new knowledge on the design of efficient catalytic converters in the context of real driving operation. Particularly, the effects of cell design parameters on the residence time and diffusion towards the active sites as well as the inhibition or the thermal response are understood.

2. Catalytic converter model

A lumped model for flow-through catalytic converters [23] was applied in this work to describe the impact of the channel geometry, washcoat loading and cell density on the CO and HC conversion efficiency. The mass flow, the inlet gas composition, pressure and temperature are imposed as boundary conditions. Based on the lumped approach, the solution of the mass and energy balances between the inlet and outlet sections of the monolith provide the outlet gas temperature, velocity and composition every time-step. These outlet gas properties depend upon the substrate wall temperature, which controls the gas-to-wall heat transfer and the chemical kinetics of the pollutant conversion.

Therefore, the heat transfer processes are solved by applying a lumped nodal approach, which is sketched in Figure 1. It is adapted from a 1D concept [24] to account for the gas to wall heat exchange, the heat losses towards environment and the thermal inertia of the monolith substrate and the external canning.

The model is based on the solution of the general heat transfer equation by explicit centered finite differences, as described in detail by Piqueras et al. ([23]). From the nodal scheme shown in Figure 1, the substrate temperature variation per time-step is obtained as

$$\Delta T_w = \frac{\Delta t}{C_{w+wc}} \left(\sum_i \frac{T_i - T_w}{R_i} + \dot{q}_r \right), \tag{1}$$

where Δt represents the time-step, T_i is the temperature of the neighbouring node i (gas and internal canning surface) and R_i represents the linking thermal resistance between the node i and the substrate. The substrate thermal inertia is taken into account by the definition of the thermal capacitance (C_{w+wc}), which is computed considering both the substrate and the washcoat. It is detailed
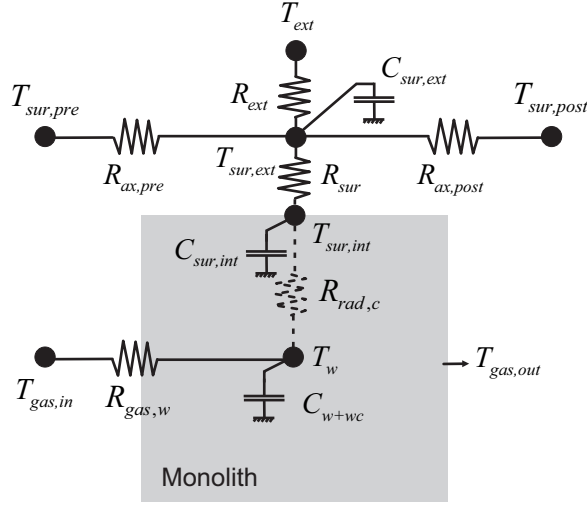
4

Figure 1: Nodal scheme of the heat transfer model.

in Section 3 for each channel geometry. The thermal power released in the chemical reactions taking place within the substrate is represented by $\dot{q}_r$.

The conversion efficiency of the gaseous pollutants is calculated by solving the transport equations applied to the chemical species along the monolith. The oxidation of CO and HC as well as the physisorption of HC on the zeolites present in the washcoat are considered in this work as abatement mechanisms. Assuming quasi-steady flow within the monolith and the washcoat [25], the one-dimensional conservation equations for the pollutant gaseous species n can be written in the bulk gas and washcoat regions respectively as [26]:

$$u_{in}\frac{\partial X_n}{\partial x} = -S_{p,gas}k_{m,n}\left(X_n - X_{n,wc}\right) \tag{2}$$

$$\sum_i \nu_{i,n}R_i + S_{p,wc}k_{m,n}\left(X_n - X_{n,wc}\right) = 0 \tag{3}$$

The bulk-gas transport equation (Eq. (2)) describes the convective transport of CO and HC along the monolith channels and their diffusion towards the washcoat interface. Analogously, Eq. (3) considers the diffusion from the washcoat interface to its internal volume, where the reaction takes place. The diffusion rates are controlled by the mass transfer coefficient and the specific

5

surfaces in every region, which are defined in Section 3 for each cell geometry. The mass transfer coefficient is determined by the cell hydraulic diameter and the flow properties as

$$k_{m,n} = \frac{D_{m,n}\text{Sh}_n}{D_h}, \tag{4}$$

where $D_{m,n}$ is the molecular diffusivity and the Sherwood number is calculated as [27]:

$$\text{Sh}_n = \text{Sh}_\infty \left(1 + \frac{0.095 D_h \text{ReSc}_n}{L_{mon}}\right)^{0.45} \tag{5}$$

On the other hand, the summation of reaction rates in Eq. (3) includes all the reactions where the pollutant species n is involved. The oxidation of CO and HC was modelled according to

$$R_{ox,n} = \eta_{int,ox,n}\frac{k_{ox,n}}{G_{ox}}X_{O_2}X_{n,wc}, \tag{6}$$

where $k_{ox,n}$ is the kinetic constant defined by the Arrhenius equation and G_{ox} represents the inhibition term for CO and HC oxidation, which was calculated as proposed by Oh and Cavendish [28].

The calculation of the HC reaction rate was completed with the modelling of the adsorption and desorption process, which is depending on the kinetic term and the amount of adsorbed HC:

$$R_{ads,HC} = \eta_{int,ads,HC}k_{ads,HC}\left(1 - \theta_{HC}\right)\psi_{HC}X_{HC,wc} \tag{7}$$

$$R_{des,HC} = k_{des,HC}\theta_{HC}\psi_{HC} \tag{8}$$

The limitations due to internal pore diffusion are included in the definition of the reaction rates to account for the impact of local concentration gradients caused by the presence of pores [29] as well as the differences in mass transfer between the bulk gas and the washcoat [30]. In this work, the classical internal pore diffusion efficiency is used [31]. This is defined as the ratio between the effective overall reaction rate and the reaction rate that would result if the entire interior surface were exposed to the external washcoat surface conditions [32]. Assuming isothermal washcoat [33] and defining the Thiele modulus for a washcoat slab geometry [34], the internal pore diffusion efficiency of each reaction is obtained as proposed by Aris [35].

6

The pollutant mole fraction at the monolith outlet is obtained from the combined solution of the chemical species conservation equations in explicit form [36]. Considering zero-order (HC desorption) and first-order reactions (CO/HC oxidation and HC adsorption), the washcoat mole fraction of species n is expressed as a linear function of the bulk gas mole fraction rearranging Eq. (3):

$$X_{n,wc} = a_n X_n + b_n \tag{9}$$

The slope and independent terms in Eq. (9) are defined as

$$a_n = \frac{S_{p,wc} k_{m,n}}{S_{p,wc} k_{m,n} - \sum_j \nu_{j,n} R_{j,n}^{1'}} \tag{10}$$

$$b_n = \frac{\sum_i \nu_{i,n} R_i^0}{S_{p,wc} k_{m,n} - \sum_j \nu_{j,n} R_{j,n}^{1'}}, \tag{11}$$

being R_i^0 the reaction rate of a zero-order reaction and $R_{j,n}^{1'}$ the reaction rate of a first-order reaction divided into the washcoat mole fraction of species n. Both a_n and b_n are constant within the control volume if the O_2 mole fraction variation is assumed negligible along it. When the available O_2 at the catalyst inlet is in clear excess, i.e. its content is much higher than that required for the complete oxidation of HC and CO, the length of the control volume can be imposed equal to the monolith length. In other words, the lumped approach, which was applied in this work, is valid regarding the assumption of constant O_2 mole fraction along the monolith. As observed in Figure 2, this condition was fulfilled in the tested WLTC taken as reference for the study. The minimum O_2 mole fraction at the monolith inlet was 0.026 and its variation along the catalyst was negligible during the whole test with respect to the engine-out content. Therefore, after combining Eq. (9) and the chemical species conservation equation in the bulk gas, the tailpipe (i.e. catalyst outlet) gas mole fraction is determined integrating into the time-step along the monolith length:

$$X_{n,out} = \frac{\left((1 - a_n) X_{n,in} - b_n\right) e^{-S_{p,gas} k_{m,n}(1-a_n)\tau} + b_n}{1 - a_n} \tag{12}$$
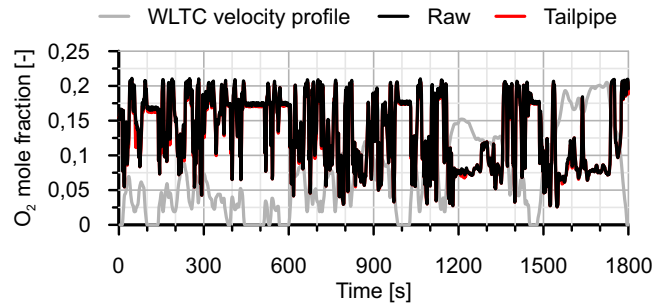
7

Figure 2: Comparison between raw and tailpipe O_2 mole fraction along the WLTC test.

Once the CO and HC mole fraction are known at the monolith outlet, the gas composition can be determined by stoichiometry. In turn, the variations in mole fraction and surface coverage define the thermal power released onto the washcoat, which couples the reaction mechanism solver with the heat transfer modelling [23].

3. Cell cross-section geometry influence on model parameters

The following assumptions have been considered to study the influence of channel geometry and washcoat loading on the catalytic conversion of pollutant emissions for square and triangular cells (sketched in Figure 3):

- The lumped flow and monolith thermal solution in Section 2 imply that all monolith channels have the same cross-section geometry concerning substrate and washcoat layer as well as they have the same thermofluid behaviour.

- The fillet radius of the substrate is zero. Consequently, perfect corners in square and triangular cross-sections are obtained from the point of view of the bare substrate.

- The washcoat layer thickness in the corners of the cross-section is up to two orders of magnitude higher than the thickness in the sides of the channel [37]. Therefore, the washcoat layer is located in the corners of the substrate and defined by a fillet radius R_f. The thickness of the washcoat layer in the centre of the cell walls is zero.

8

- The washcoat deposition is uniform along the channel length. The washcoat micro-structure (porosity, pore size and tortuosity) and active sites distribution are uniform. These assumptions are compatible with the uniform reaction rate defined in the lumped flow solver.
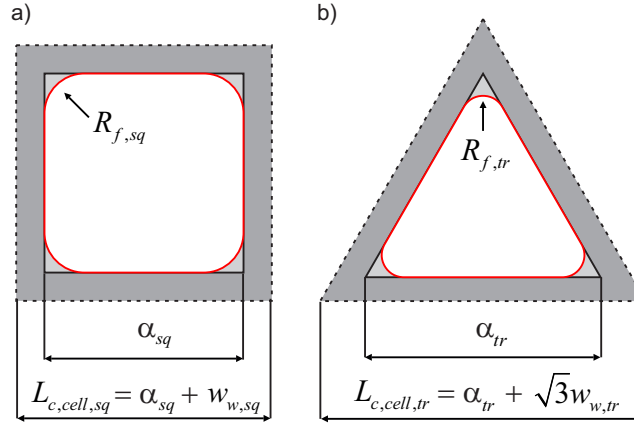
- The triangle cells are equilateral [38].

Figure 3: Substrate and washcoat distinction in (a) square and (b) triangular cross-sections.

The main parameter defined by the cell meso-geometry with influence on the pollutants conversion efficiency is the specific surface. As shown in the conservation equations for chemical species applied to the bulk gas (Eq. (2)) and washcoat (Eq. (3)) regions, two specific surfaces are distinguished:

- The gas specific surface defined as the ratio of catalytic surface to the gas volume. This is ultimately governed by the monolith specific surface ($S_{p,mon}$) to open frontal area (OFA) ratio:

$$S_{p,gas} = \frac{S_{cat}}{V_{gas}} = \frac{S_{cat}}{V_{mon}\frac{S_{gas}}{S_{cell}}} = \frac{\frac{S_{cat}}{V_{mon}}}{\frac{S_{gas}}{S_{cell}}} = \frac{S_{p,mon}}{OFA} \qquad (13)$$

- The washcoat specific surface defined as the ratio between the catalytic surface and the washcoat volume. Considering the cell, solid and washcoat cross-section areas, the washcoat specific surface is expressed as

9

$$S_{p,wc} = \frac{S_{cat}}{V_{wc}} = \frac{S_{cat}}{V_{mon} \frac{S_{w+wc}}{S_{cell}} \frac{S_{wc}}{S_{w+wc}}} = \frac{\frac{S_{cat}}{V_{mon}}}{(1 - \frac{S_{gas}}{S_{cell}}) \frac{S_{wc}}{S_{w+wc}}} = \frac{S_{p,mon}}{(1 - OFA)\Theta_{wc}},$$

(14)

where Θ_{wc} represents the washcoat fraction over the solid cross-section area.

The expressions to calculate the specific surfaces previously defined as a function of the cell meso-geometry are shown in Table 1. The influence of the channel width, wall thickness and washcoat fillet radius has been made explicit to clearly distinguish between square and triangular shapes.

The cell geometry also affects the mass and heat transfer. As previously described in Eq. (4), the Sherwood number is computed as a function of the cell geometry and the flow properties [27], being Sh_∞ equal to 2.976 for square cells and 2.496 for triangular cells. The same approach is applied to determine the heat transfer coefficient:

$$h = \frac{\kappa_{gas} Nu}{D_h}$$

(15)

$$Nu = Nu_\infty \left(1 + \frac{0.095 D_h Re Pr}{L_{mon}}\right)^{0.45}$$

(16)

$$D_h = 4 \frac{OFA}{S_{p,mon}}$$

(17)

In Eq. (16), Nu_∞ takes the same values as Sh_∞. These expressions evidence the influence of the hydraulic diameter on the calculation of the Re, Nu, Sh, $k_{m,n}$ and h. Therefore, the impact of the cell meso-geometry on the transfer coefficients is added to that on the specific surfaces.

The thermal response of the monolith is also influenced by the monolith thermal capacitance and the radial conductivity towards the external metal can. The thermal capacitance for square and triangular cells is given by:

Table 1: Specific surfaces definition as a function of the cell meso-geometry.

	Square	Triangular
$L_{c,cell}$	$\alpha + w_w$	$\alpha + \sqrt{3}w_w$
σ	$\dfrac{1}{L_{c,cell}^2}$	$\dfrac{4}{\sqrt{3}L_{c,cell}^2}$
OFA	$\dfrac{\alpha^2 - (4-\pi)R_f^2}{L_{c,cell}^2}$	$\dfrac{\alpha^2 - 4\left(3 - \frac{\pi}{\sqrt{3}}\right)R_f^2}{L_{c,cell}^2}$
Θ_{wc}	$\dfrac{(4-\pi)R_f^2}{L_{c,cell}^2 - \alpha^2 + (4-\pi)R_f^2}$	$\dfrac{4\left(\sqrt{3}\pi - 9\right)R_f^2}{4\left(\sqrt{3}\pi - 9\right)R_f^2 - 6\sqrt{3}L_{c,cell}w_w + 9w_w^2}$
$S_{p,mon}$	$\dfrac{4\alpha - 2(4-\pi)R_f}{L_{c,cell}^2}$	$\dfrac{4\sqrt{3}L_{c,cell} + \frac{8}{3}\left(\sqrt{3}\pi - 9\right)R_f - 12w_w}{L_{c,cell}^2}$
$S_{p,gas}$	$\dfrac{4\alpha - 2(4-\pi)R_f}{\alpha^2 - (4-\pi)R_f^2}$	$\dfrac{2\left(2\sqrt{3}L_{c,cell} + \left(\sqrt{3}\pi - 12\right)R_f - 6w_w\right)}{\alpha^2 + \frac{4}{3}\left(\sqrt{3}\pi - 9\right)R_f^2}$
$S_{p,wc}$	$\dfrac{2\left((\pi - 4)R_f + 2\alpha\right)\left((\pi - 4)R_f^2 - (1 + 2\alpha)w_w\right)}{(4-\pi)R_f^2\left((\pi-4)R_f^2 - 2\alpha w_w - w_w^2\right)}$	$\dfrac{3\left(2\sqrt{3}L_{c,cell} + \left(\sqrt{3}\pi - 12\right)R_f - 6w_w\right)}{2\left(\sqrt{3}\pi - 9\right)R_f^2}$

$$C_{w+wc,sq} = \left(4\left(\alpha + \frac{w_w}{2}\right)\frac{w_w}{2}\rho_w c_{p,w}\left(1 - \varepsilon_w\right) + \right.$$
$$\left. + \left(4 - \pi\right)R_f^2 \rho_{wc} c_{p,wc}\left(1 - \varepsilon_{wc}\right)\right)L_{mon} \tag{18}$$

$$C_{w+wc,tr} = \left(3\left(\alpha + \frac{\sqrt{3}}{2}w_w\right)\frac{w_w}{2}\rho_w c_{p,w}\left(1 - \varepsilon_w\right) + \right.$$
$$\left. + \left(3\sqrt{3} - \pi\right)R_f^2 \rho_{wc} c_{p,wc}\left(1 - \varepsilon_{wc}\right)\right)L_{mon} \tag{19}$$

The radial conductivity of the monolith is determined from the cell geometry and the substrate and gas conductivity [39]. This approach is based on the determination of the equivalent thermal resistance by conduction between adjacent cells. The thermal resistance scheme across the porous wall is shown in Figure 4 for each cell shape. Defining each thermal resistance per unit of length in the axial direction, the radial conductivity is obtained as the inverse of the equivalent thermal resistance. Its particular solution for square and triangular channels is as follows:

$$\kappa_{rad,sq} = \left(\frac{w_w}{\kappa_w\left(\alpha + w_w\right)} + \frac{\alpha}{\kappa_{gas}\alpha + \kappa_w w_w}\right)^{-1} \tag{20}$$

$$\kappa_{rad,tr} = \left(\frac{\alpha - \sqrt{3}w_w}{\left(\sqrt{3}\alpha - 3w_w\right)\kappa_{gas} + 6w_w\kappa_w} + \right.$$
$$\left. + \frac{4\sqrt{3}w_w\left(\kappa_w + \kappa_{gas}\right)}{6w_w\left(\kappa_w^2 - \kappa_{gas}^2\right) + 3w_w\kappa_w\kappa_{gas} + 2\sqrt{3}\alpha\left(\kappa_w\kappa_{gas} + \kappa_{gas}^2\right)}\right)^{-1} \tag{21}$$

The cell geometry also affects the mechanical performance of the monolith. It is evaluated by means of the thermal and mechanical integrity factors [20], which are defined in Table 2. The TIF_w is directly related to the maximum temperature gradient that the monolith can withstand when exposed to thermal cycles. In addition to this, the MIF_w, which is inversely proportional to the TIF_w, represents the contribution of the cell geometry to the load carrying limit along the diagonal and parallel to the wall.
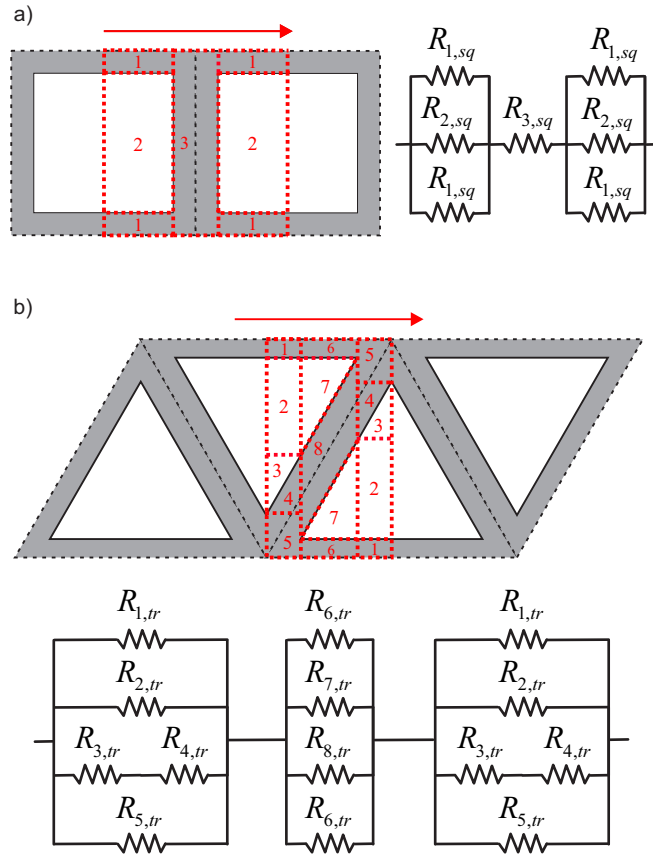
12

Figure 4: Scheme of the equivalent conduction thermal resistance between adjacent (a) square and (b) triangular cells.

Table 2: Catalyst parameters as a function of the cell meso-geometry.

	Square	Triangular
TIF_w	$\dfrac{L_{c,cell}}{w_w}$	$\dfrac{2}{\sqrt{6}}\dfrac{L_{c,cell}}{w_w}$
MIF_w	$\dfrac{w_w}{\alpha TIF_w}$	$\dfrac{4w_w}{\sqrt{6}\alpha TIF_w}$

4. Definition of the study

The performance of a commercial oxidation catalyst with square cells, whose main characteristics are shown in Table 3, was taken as baseline for the theoretical analysis of the cell ge-

13

ometry influence on the pollutant conversion efficiency. The catalytic converter was installed in a passenger car diesel engine. As summarized in Table 4, the engine was equipped with variable geometry turbine (VGT) and high- and low-pressure cooled exhaust gas recirculation (EGR). The high-pressure EGR line extracted the gases from the exhaust manifold through the cylinder head. Instead, the low-pressure EGR line extracted the gases at the outlet of the wall-flow particulate filter placed downstream of the analysed oxidation catalyst and drove them towards the compressor inlet.

Table 3: Main parameters of the baseline catalytic converter.

Substrate material	Cordierite
Catalyst	Pt & Zeolite
Diameter [m]	0.172
Length [m]	0.082
Cell shape [−]	Square
Number of channels [−]	14400
Cell density [cpsi]	400
Channel width [mm]	1.169
Wall thickness [mm]	0.101
Washcoat fillet radius [mm]	0.584

The engine was coupled to an asynchronous dynamometer that allowed for the control of the engine speed and torque during the WLTC test. The air and fuel mass flows were recorded by means of a flow meter and a gravimetric balance respectively. The gaseous emissions were measured at the oxidation catalyst inlet and outlet with a HORIBA MEXA-7160 DEGR. This gas analyser was also used to determine the EGR rate measuring the CO_2 content in the exhaust gas upstream of the oxidation catalyst and in the intake manifold. During the WLTC, high-pressure EGR operated until the engine coolant temperature reached 60°C. Over this temperature, the high-pressure EGR was substituted by low-pressure EGR. The opening of the EGR valves was monitored by the engine control unit. With this information, the mass flow across the exhaust aftertreatment systems was calculated. Finally, pressure and temperature sensors were placed at key

14

Table 4: Main characteristics of the engine.

Engine type	HSDI Diesel
Number of cylinders [-]	4 in line
Number of valves [-]	4 per cylinder
Displaced volume [cc]	1598
Stroke [mm]	79.5
Bore [mm]	80
Compression ratio [-]	14.5:1
Maximum power [kW]	96 @ 4000 rpm
Maximum torque [Nm]	320 @ 1750 rpm
Fuel injection	Common-rail direct fuel injection
Turbocharger	VGT
EGR	Cooled high- and low-pressure

locations of the intake and exhaust lines. In particular, pressure and temperature were measured upstream and downstream of the oxidation catalyst. Table 5 describes the main instrumentation used in this work.

Table 5: Main characteristics of the instrumentation.

Magnitude	Instrument	Range	Accuracy
Crank angle	Kistler encoder	0-360°	±0.02 CAD
Torque	Dynamometer	0-400 Nm	±0.5 Nm
Air mass flow	Sensiflow DN80	20-720 kg/h	±2%
Fuel mass flow	Gravimetric balance	0-150 kg/h	±0.2%
Temperature	K-type thermocouple	70-1520 K	±2 K
Mean pressure	Kistler piezo-resistive sensor	0-10 bar	linearity 0.2%

The WLTC test was run twice at room temperature (20°C). Once the first WLTC was finished, an active particulate filter regeneration was performed. After that, the engine was conditioned back to room temperature over a 24 h period before running the second WLTC. Figure 5 shows the

15

experimental CO and HC emissions and their conversion efficiencies during the WLTC compared to the modelling results. The experimental results correspond to the average of the two performed tests. Therefore, the error bars represent the amount of spread between the two experimental results. The two tests were in good agreement and high repeatability in emissions, and hence in conversion efficiency. As observed in Figure 5(a), most of the HC raw emission took place during the low and medium velocity WLTC phases. Nevertheless, the cumulative HC conversion efficiency was kept around 90% in every WLTC phase (Figure 5(c)). This high HC conversion efficiency was due to the combination of HC adsorption at low temperature and oxidation as the catalyst temperature increased. Figure 5(b) shows that the CO raw emission reached its maximum during the high velocity WLTC phase, mainly due to high CO raw emission peaks during fast accelerations. High pre-catalyst CO mole fraction self-inhibited CO oxidation within the catalyst. Thus, the CO conversion efficiency scarcely overcame 50% during the extra high phase of the cycle (Figure 5(d)), despite of the high gas temperature (Figure 5(e)).

The catalytic converter model was calibrated with a set of steady-state tests run at various engine speeds and loads covering the low to medium exhaust temperature range. These tests were monitored in a continuous way to account for the thermal transient effects, as described in detail by Payri *et al.* [36]. The resulting calibration was applied to the driving cycle and refined iteratively. The main parameters defining the chemical response of the catalytic converter, as described in Section 2, are provided in Table 6. This setup was kept constant for the theoretical analysis of the monolith response as a function of the cell geometry. As observed in Figure 5, the model was able to capture the CO and HC depletion rate with high accuracy based on the prediction of the flow transport and the thermal transient response undergone within the catalytic converter. Thus, the calculated catalyst conversion efficiency fell within the range of the measured values in almost every WTLC phase for both CO and HC. Table 7 shows the absolute error in cumulative CO and HC conversion efficiency in every WLTC phase as the difference between modelled and experimental data. The relative error is also provided. It is obtained as the absolute error divided into the experimental conversion efficiency for every WLTC phase and pollutant. As observed, the maximum absolute error for CO is obtained in the low speed phase but is kept below 2.5%. It corresponds to relative error equal to 5.59%. This was because the experimental CO conversion
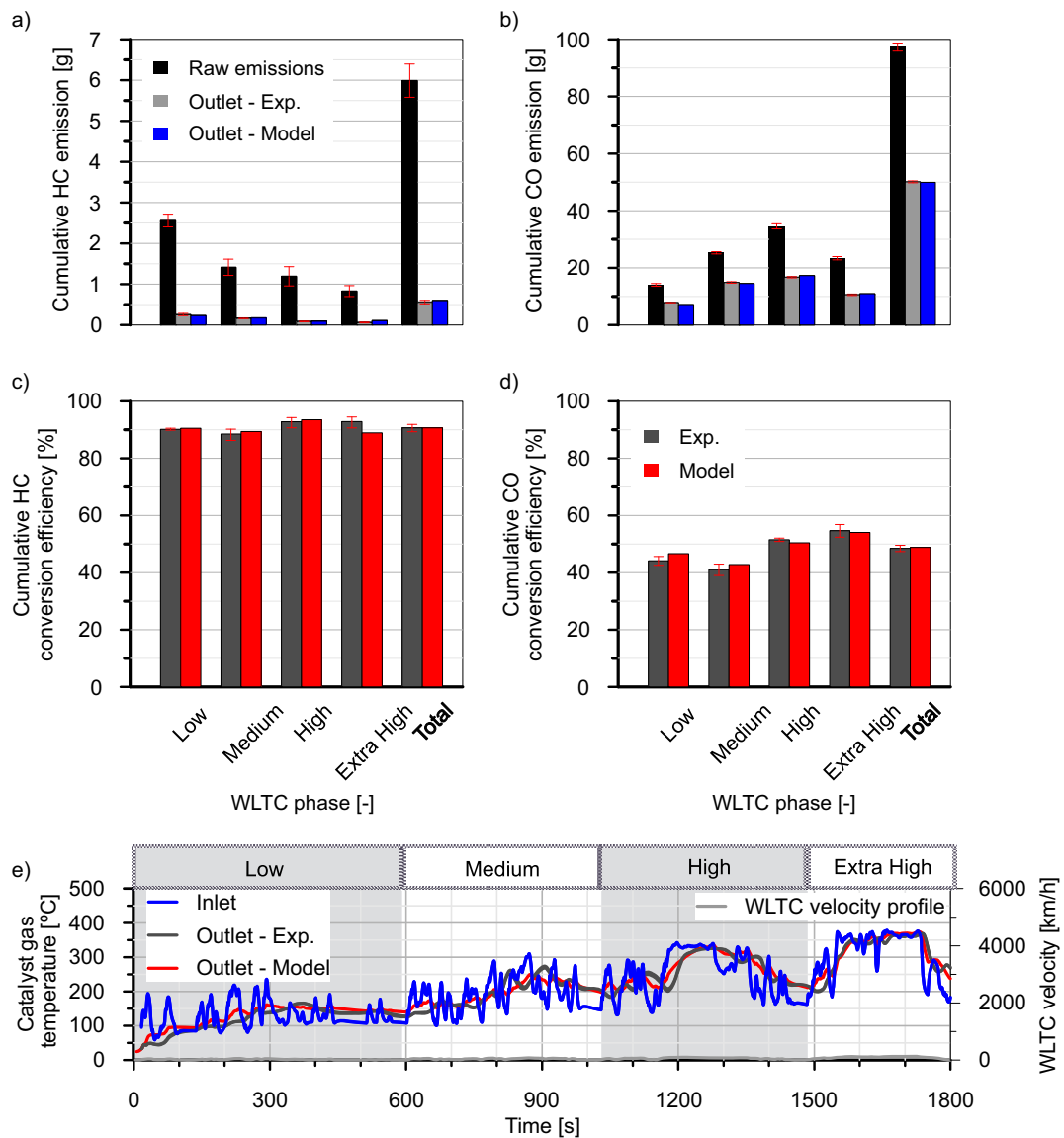
16

Figure 5: Comparison between experimental and modelling results along the WLTC phases: Cumulative raw and tailpipe (a) HC and (b) CO emissions; Cumulative (c) HC and (d) CO conversion efficiency; and (e) catalyst inlet and outlet gas temperature.

efficiency was very high during the first seconds of the WLTC despite it rapidly converged to the expected low values (please see Figure 9(a)). Most probably, this experimental deviation with respect to the model results was due to measurement uncertainties related to the very low cumulative CO mass emission at the beginning of the test. In the case of HC, the maximum

17

absolute error is below 4% (4.25% in relative error). The absolute and relative errors for the whole WLTC are below 1% for CO and HC. It indicates that all the phenomena are modelled in a balanced way, which leads to a good representation of the real catalyst response WLTC phase after phase even under the very complex driving operating conditions.

Table 6: Calibration of the oxidation catalyst model.

Kinetic constants		
	P_f [−]	E_a [J/mol]
CO oxidation	3×10^{17}	78000
HC oxidation	20×10^{17}	89000
HC adsorption	1.8	0
HC desorption	5000	95000

Table 7: Assessment of absolute and relative errors in cumulative CO and HC conversion efficiency between modelled and experimental data in every WLTC phase.

	Low	Medium	High	Extra High	Total
Absolute error					
CO	−2.47%	−1.80%	1.08%	0.61%	−0.33%
HC	−0.35%	−0.89%	−0.70%	3.94%	0.01%
Relative error					
CO	−5.59%	−4.39%	2.10%	1.12%	−0.69%
HC	−0.39%	−1.01%	−0.76%	4.25%	0.01%

These trends in cumulative error at the end of every WLTC phase are confirmed applying the three-sigma rule [40] to the cumulative conversion efficiency of CO and HC and the oxidation catalyst outlet temperature evaluated with a frequency of 1 Hz. The three-sigma rule establishes three ranges around the mean value (μ). The first one contains the values between $[\mu - \sigma_e; \mu + \sigma_e]$, i.e. the 68.27% of the results assuming a normal distribution. The next interval is larger and covers 95.45% of the data between $[\mu - 2\sigma_e; \mu + 2\sigma_e]$. Finally, the band around the mean with a half-width of three times the standard deviation $[\mu - 3\sigma_e; \mu + 3\sigma_e]$ adds up to 99.73%

of the values, so that almost all the simulation results will be within this last prediction interval. Therefore, every interval quantifies the error within a different probability of certainty. Figure 6 shows the results concerning absolute error (in modulus). As observed in Figure 6(a), the $2\sigma_e$ error (95.45% of the data) in oxidation catalyst outlet gas temperature reached 36°C, but the $1\sigma_e$ error (68.27% of the data) was scarcely 16°C. In addition, all WLTC phases were modelled with similar accuracy. Figure 6(b) depicts the results corresponding to the cumulative CO conversion efficiency. In this case, $2\sigma_e$ absolute error was very low (below 5%) despite $3\sigma_e$ (99.73% of the data) increased to 40% because of the differences at the very beginning of the cycle produced by spurious measurements. In the case of HC, the results were even better being $2\sigma_e$ absolute error equal to 2.25% and $3\sigma_e$ one below 4.75%.

On this basis, the parametric study consisted of a sweep in washcoat loading for square and triangular cells. The washcoat loading was varied by means of the fillet radius definition. According to the listed assumptions in Section 3, the maximum fillet radius involves a circular effective cross-section for the bulk gas, as defined in Figure 7.

Once the most promising washcoat loading was identified, the cell density was varied from 200 cpsi to 800 cpsi for ceramic and metallic substrates with square and triangular cells. An additional condition is required to set the change in channel width and wall thickness as the cell density is varied. As a second boundary, constant open frontal area of the substrate (OFA_w) was imposed. It is computed assuming $R_f = 0$, i.e. no washcoat, from the OFA definition. The OFA_w corresponding to the baseline monolith (0.847) was selected. In turn, this boundary condition means that constant TIF_w was also imposed. Taking into account that the channel width to wall thickness ratio is known from the TIF_w definition, i.e.

$$\left.\frac{\alpha}{w_w}\right|_{sq} = TIF_{w,sq} - 1 \tag{22}$$

$$\left.\frac{\alpha}{w_w}\right|_{tr} = \frac{\sqrt{6}}{2}TIF_{w,tr} - \sqrt{3}, \tag{23}$$

the cell density and the TIF_w are related in each cell geometry:
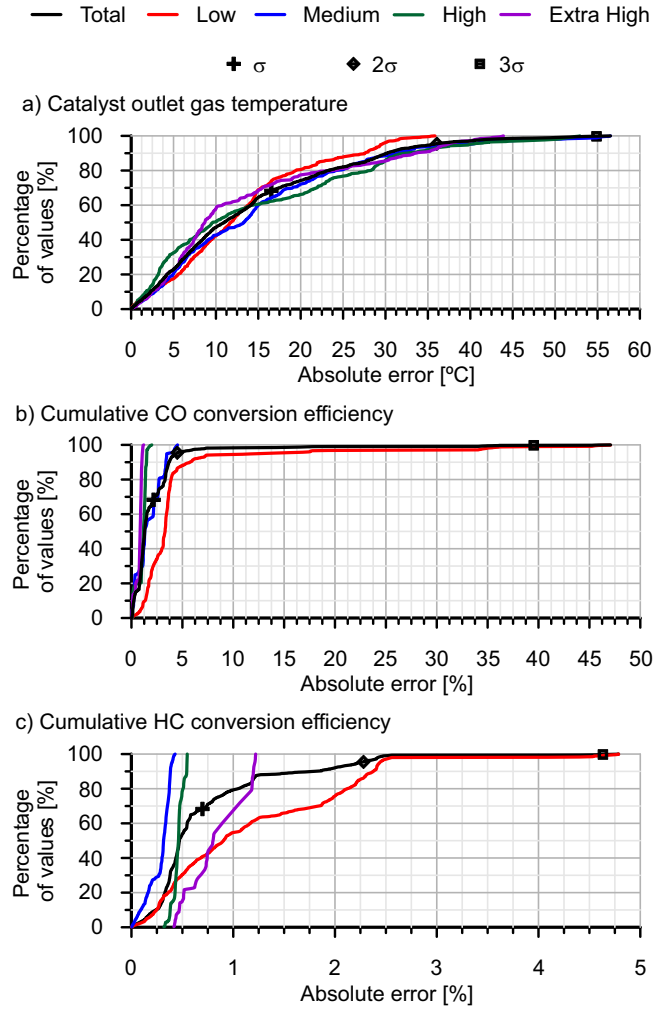
19

Figure 6: Absolute error in modulus bewteen modelled and experimental data along the WLTC applying the three-sigma rule: (a) Catalyst outlet gas temperature, (b) cumulative CO conversion efficiency and (c) cumulative HC conversion efficiency.

$$OFA_{w,sq} = \frac{\alpha_{sq}^2}{L_{c,cell,sq}^2} = \frac{\alpha_{sq}^2}{TIF_{w,sq}^2 w_{w,sq}^2} = \frac{\left(TIF_{w,sq} - 1\right)^2}{TIF_{w,sq}^2} \qquad (24)$$

$$OFA_{w,tr} = \frac{\alpha_{tr}^2}{L_{c,cell,tr}^2} = \frac{4\alpha_{tr}^2}{6TIF_{w,tr}^2 w_{w,tr}^2} = \frac{\left(TIF_{w,tr} - \sqrt{2}\right)^2}{TIF_{w,tr}^2} \qquad (25)$$
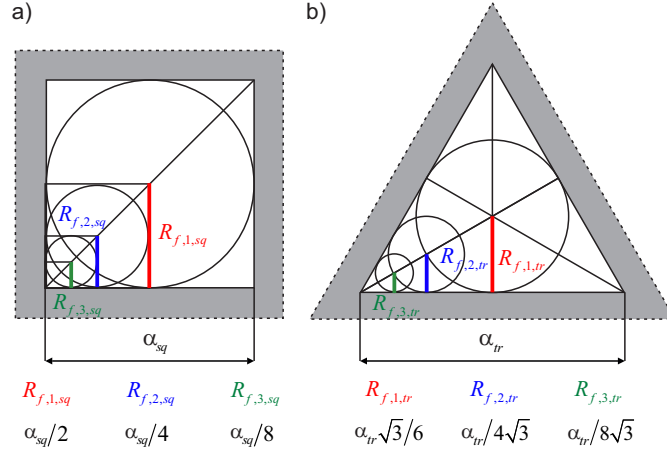
20

Figure 7: Graphical fillet radius definition in (a) square and (b) triangular cells.

According to Eqs. (24) and (25), the TIF_w is 12.58 and 17.8 for the square and triangular cells respectively. Once the TIF_w was defined, the wall thickness was determined according to the selected cell density:

$$\sigma_{sq} = \frac{1}{L_{c,cell,sq}^2} = \frac{1}{w_{w,sq}^2 TIF_{w,sq}^2} \rightarrow w_{w,sq} = \frac{1}{\sqrt{\sigma_{sq}} TIF_{w,sq}} \tag{26}$$

$$\sigma_{tr} = \frac{1}{L_{c,cell,tr}^2} = \frac{2}{3w_{w,sq}^2 TIF_{w,tr}^2} \rightarrow w_{w,tr} = \frac{\sqrt{2}}{\sqrt{3\sigma_{tr}} TIF_{w,tr}}, \tag{27}$$

Finally, the channel width was obtained by applying Eqs. (22) and (23). In addition, according to the definitions presented in Table 2, the MIF_w was also kept constant as the cell density was varied. Therefore, the cell density swept at constant OFA_w avoids variations in the mechanical integrity of the monolith design.

5. Results and discussion

Figure 8 shows the effect of cell density, shape and washcoat loading on the main catalyst geometrical parameters. Plot (a) in Figure 8 depicts the OFA. As observed, the triangular cells show higher penalty in effective open frontal area, specially as the fillet radius increases. The corresponding channel width and wall thickness are represented in Figure 8(b) and (c) respectively.

21

As expected, both parameters decrease with the cell density, with higher channel width at the expense of thinner wall in the triangular cells with respect to the square ones.
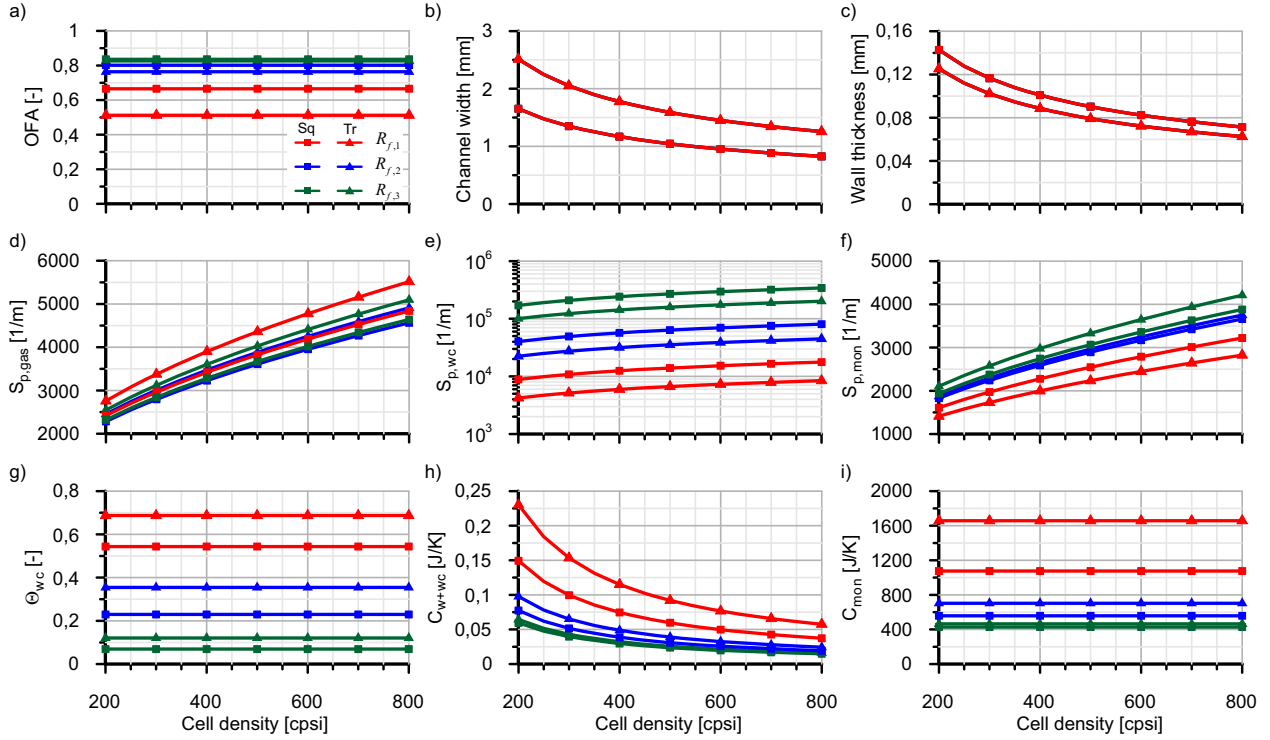

Figure 8: Dependence of meso-geometry parameters on the cell density, shape and washcoat loading.

Figure 8(d) and (e) represent the specific surfaces related to bulk gas and washcoat. Although increasing the gas specific surface is commonly reported as positive in the literature, the washcoat specific surface impact is put aside. High gas specific surface favours the conversion efficiency (Eq. (12)). However, low washcoat specific surface increases the pollutants washcoat mole fraction, as directly obtained from Eq. (9). As a result, an increase of the reaction rate is obtained.

The conversion efficiency is more sensitive to the gas specific surface variation than to the change in washscoat specific surface, as discussed in the following sections. However, the washcoat adds a synergistic or opposite effect depending on the cell geometry definition. As observed, the specific surfaces are increased as the cell density does. However, an increase in the fillet radius leads to higher gas specific surface but to lower washcoat specific surface, i.e. provides a combined benefit in conversion efficiency. Comparing cell shapes at the same cell density, the

22

triangular shape provides higher gas specific surface than the square one, as shown in Figure 8(d). By contrast, the washcoat specific surface is mainly set by the washcoat loading, being lower for the triangular cell with respect to square cell once both are compared at equivalent fillet radius. Therefore, better performance is expected for triangular cells in comparison to square ones from the specific surfaces point view.

The trends in gas and washcoat specific surfaces are dictated by the OFA, the monolith specific surface and the washcoat fraction over the solid cross-section area, as described by Eqs. (13) and (14). These last two parameters are shown in Figure 8(f) and (g). The monolith specific surface increases with the cell density and the decrease of the washcoat loading. However, the washcoat fraction over the solid cross-section area is constant with the cell density, but it shows a clear dependency on the cell shape and the washcoat loading. As shown in Figure 8(g), the washcoat fraction over the solid cross-section area is higher in triangular cells than in square ones and increases as the fillet radius does.

The meso-geometry parameters also play a relevant role in the dynamics of the thermal response. Despite the very different thermal capacitance per channel as a function of the cell density (Figure 8(h)), the monolith thermal capacitance (Figure 8(i)) is kept constant with cell density. The reason is that the OFA is constant with cell density, as well as the monolith volume. Consequently, the solid area is also constant independently of the cell density, and hence the thermal capacitance.

The differences in monolith thermal capacitance among cell geometries are due to the washcoat loading. As stated in the definition of study section, constant OFA_w was set as a boundary condition for all geometries. Therefore, the substrate volume is the same in all the computed cases. As a consequence, the highest monolith thermal capacitance corresponds to the triangular cell with the maximum fillet radius, i.e. to the cross-section geometry with the highest washcoat fraction, as represented in Figure 8(h). In fact, the washcoat fraction over the solid cross-section area determines the trend in monolith thermal capacity.

Although the transient response of the catalyst is usually related to the monolith thermal capacity via the light-off factor [41], the dynamics of the thermal transient is also very dependent on the monolith specific surface and the radial conductivity. According to the monolith specific surface and thermal capacitance, the slowest thermal response is expected for the triangular cell

with the maximum fillet radius, followed by the square cell with the equivalent washcoat loading. A slow thermal response is detrimental during catalyst heat up (e.g. vehicle acceleration). However, whilst the catalyst is cooling down a slower thermal response becomes desirable. In parallel, the radial thermal conductivity of triangular cells is higher than that corresponding to the square geometry because of gas and substrate arrangements (0.37 vs. 0.17 W/mK). Therefore, higher heat losses towards the environment are expected in triangular cells. This is a negative characteristic, since it leads to slow warm up but fast cool down during fuel cut-off phases.

The concurrence of all these complex phenomena, related in trade-offs with different sensitivity on catalytic pollutant conversion efficiency, requires an integral assessment of the catalyst response in representative driving conditions to clear up the actual impact of each cell geometry approach.

5.1. Conversion efficiency dependence on washcoat loading

The impact of the washcoat loading on the pollutants conversion efficiency was analysed imposing the cell density of the baseline monolith (400 cpsi), whose fillet radius coincides with $R_{f,1}$. Figure 9 shows the cumulative CO and HC conversion efficiencies along the WLTC, which were obtained from cumulative engine output and tailpipe emissions. Experimental data is compared with square and triangular cells with variable washcoat loading. As observed, the experimental results are in good agreement with the model prediction corresponding to the square cell with $R_{f,1}$. The computed cases showed more sensitivity to the variation in washcoat loading than to the cell shape.

The cumulative CO conversion efficiency showed high sensitivity to the substrate temperature (Figure 10(a)) and to the instantaneous mass flow and CO mole fraction, which gave rise to the instantaneous CO mass flow shown in Figure 10(b). The main trend is such that the cumulative CO conversion efficiency shows a clear increasing rate as the substrate temperature increases. The increase in conversion efficiency is more notable below 150 °C in substrate temperature. This is due to the high CO internal pore diffusion efficiency below this threshold [23]. Beyond 150 °C, the cumulative CO conversion efficiency still increases, but at a lower rate due to very low internal pore diffusion and the greater importance of the sudden efficiency drops. Nevertheless, the lack of influence the monolith thermal capacitance imposes upon the CO conversion efficiency must
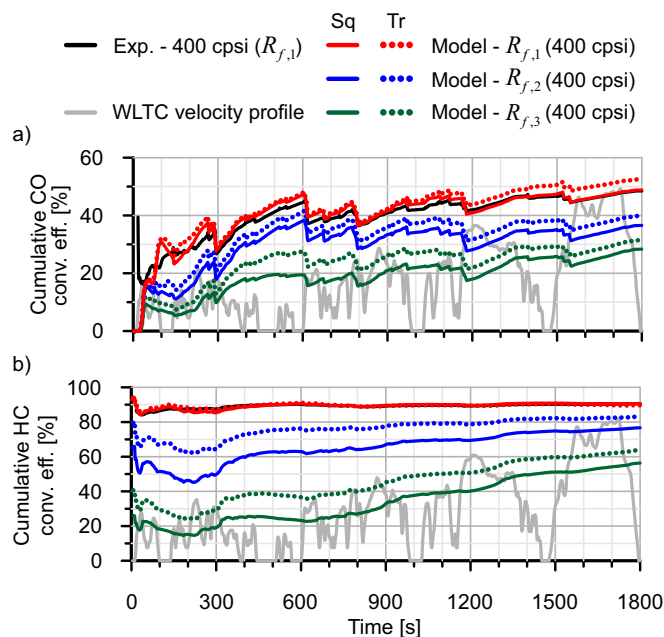
24

Figure 9: Comparison between experimental and modelling results as a function of the cell shape and the washcoat loading: (a) Cumulative CO conversion efficiency and (b) Cumulative HC conversion efficiency.

be highlighted. It impacts on substrate temperature, but not in a sufficient magnitude to affect CO conversion efficiency for the driving conditions studied here.

The observed steep drops in cumulative CO conversion efficiency (Figure 9(a)) are linked to fast accelerations. Several phenomena take place simultaneously during these phases. On the one hand, as a positive effect, the gas temperature increases. However, this effect is overcome by the catalyst thermal inertia, as observed in the substrate temperature evolution (Figure 10(a)). On the other hand, the high instantaneous CO raw emission (Figure 10(b)), which increases up to four orders of magnitude the oxidation inhibition term with respect to its mode value along the driving cycle (Figure 10(c)), deteriorates CO conversion efficiency. This together with the simultaneous decrease in residence time within the catalyst (Figure 10(d)) not only reduces instantaneous conversion efficiency but also decreases cumulative CO conversion efficiency because of its high weight with respect to the total emitted mass. The conversion efficiency penalty is very similar for all the tested cell geometries, as observed in Figure 9(a). The reason lies in the fact that the
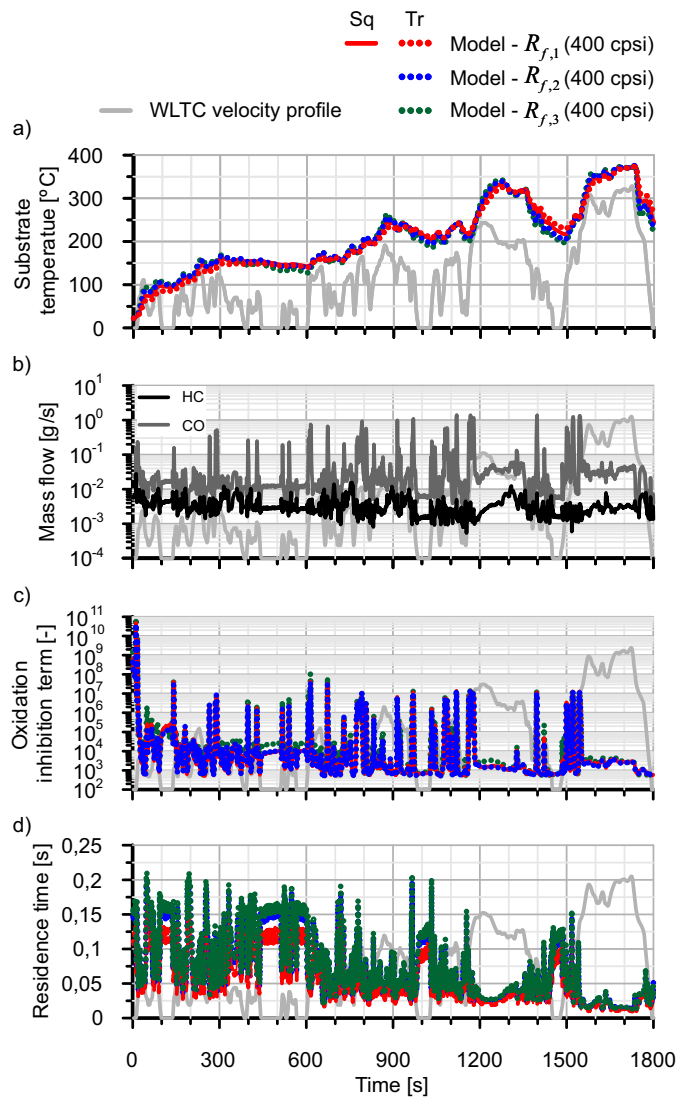
25

Figure 10: Comparison between parameters affecting the CO conversion efficiency as a function of the cell shape and the washcoat loading: (a) substrate temperature, (b) CO and HC mass flow, (c) oxidation inhibition term and (d) residence time.

effects on inhibition term and residence time of varying the cell shape and washcoat loading are negligible at constant cell density.

In order to complete the analysis of variables affected by the change in cell geometry at constant OFA, Figure 11 represents the mass transfer coefficients and the internal pore diffusion efficiency for CO and HC. Despite of the differences in hydraulic diameter between the computed

26

cell geometries, the final impact on the mass transfer coefficients is negligible. By contrast, the internal pore diffusion is much more sensitive to cell geometry. Although it shows a common trend to decrease as the temperature increases, there are evident quantitative differences among cell geometries. These differences are opposite to the ones observed in cumulative conversion efficiency. The triangular cell provides lower internal pore diffusion efficiency but higher conversion efficiency than the square cell with the same fillet radius definition. As the fillet radius decreases, the internal pore diffusion efficiency increases significantly. However, the cumulative conversion efficiency decreases substantially despite this positive trend.

This analysis justifies that the gas and washcoat specific surfaces, which are represented in Figure 8(d) and (e), are the parameters governing the trend in cumulative conversion efficiency at constant cell density and substrate OFA. Under these boundaries, the triangular shape is always favoured because of the higher gas and lower washcoat specific surfaces than the equivalent square cell. Hence, the benefit in conversion efficiency. Further to this, the reduction in gas specific surface and the increase in washcoat specific surface as the washcoat loading is decreased deteriorate the conversion efficiency.

Although the discussion has been initially focused on CO, similar trends and explanations also apply to cumulative HC conversion efficiency. Nevertheless, the HC adsorption on zeolites [26] plays an additional role during the low and medium velocity phases of the WTLC. Figure 12, which represents the contributions to the HC mole variation across the catalyst, reveals that the main HC abatement mechanism during the low velocity phase is the HC adsorption. Despite of the fact that the oxidation takes progressive importance, the adsorption is significant till the second part of the medium velocity phase for cell geometries with maximum fillet radius. The decrease in fillet radius leads to a negative snowball effect since the maximum adsorption capacity decreases. This makes the surface coverage, which is shown in Figure 12(c), increase faster. Consequently, the equilibrium moves towards the desorption, decreasing the adsorption rate and its contribution to the HC removal. These mechanisms explain the high sensitivity of the cumulative HC conversion efficiency to the washcoat loading, in parallel to the influence of the specific surfaces. In addition, this sensitivity is more marked in the square cells due to their lower washcoat fraction over the solid cross-section area.
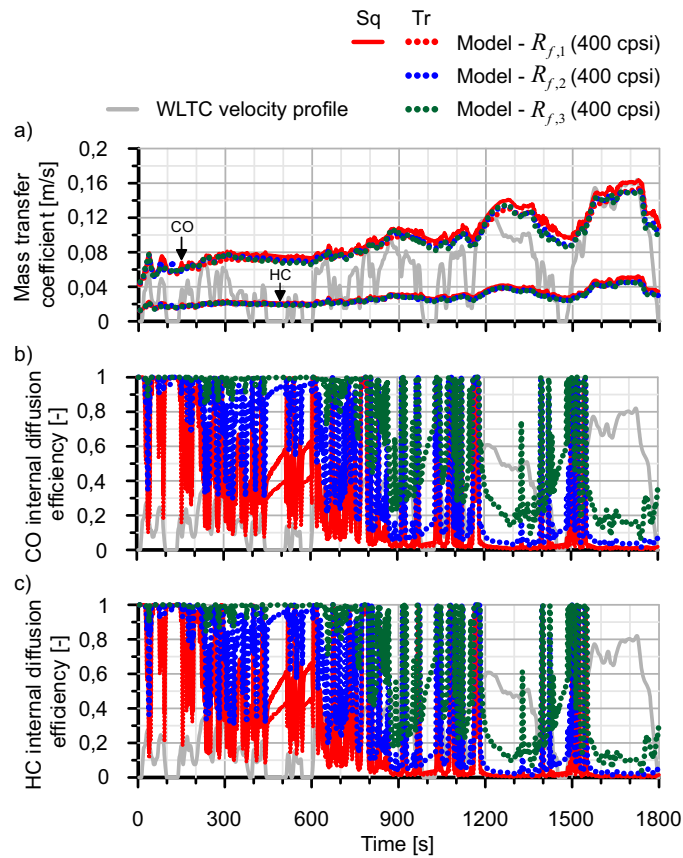
27

Figure 11: Comparison of the mass transfer parameters as a function of the cell shape and the washcoat loading: (a) CO and HC mass transfer coefficients, (b) CO internal pore diffusion efficiency and (c) HC internal pore diffusion efficiency.

5.2. Conversion efficiency dependence on cell density

The cell density was varied for the square and triangular cells keeping constant the fillet radius ($R_{f,1}$). As a result of the cell density variation at constant substrate OFA and fillet radius, the residence time, the washcoat fraction and the monolith thermal capacitance were kept constant for each cell shape, as justified by Figures 8(a), (g) and (i). Therefore, these parameters do not play any role in the sensitivity to the cell density of the cumulative conversion efficiency. Figure 13 provides a comprehensive summary of the pollutants cumulative conversion efficiency per WLTC phase and the end value as a function of the cell density. The different series are ordered for each cell density from the lowest (front) to highest (back) cumulative conversion efficiency. Besides
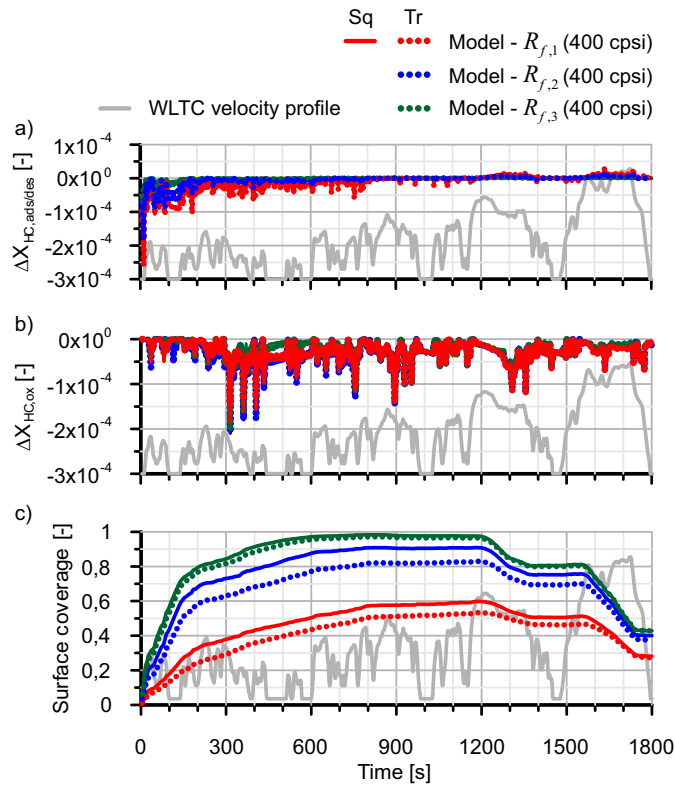
Figure 12: Contributions to HC abatement as a function of the cell shape and the washcoat loading: (a) sorption process, (b) oxidation and (c) HC surface coverage.

the results corresponding to square and triangular cells in cordierite substrates, a metallic substrate has been included for the triangular case. The triangular metallic substrate has different thermal capacitance and conductivity, which suffer a substantial increase.

As a general trend, the cumulative conversion efficiency increases as the cell density does due to the enhancement of the gas specific surface. However, the impact on the catalyst conversion efficiency is lower than the one found when the washcoat loading was varied. The increase in cell density enhances the gas specific surface but it also rises the washcoat specific surface, which partially neutralises the pollutant removal benefits provided by the bulk gas to washcoat mass transfer.

Besides the positive but limited impact of the trend in specific surfaces, the mass transfer is also benefited by the cell density increase. Taking the HC emission as example, Figure 14
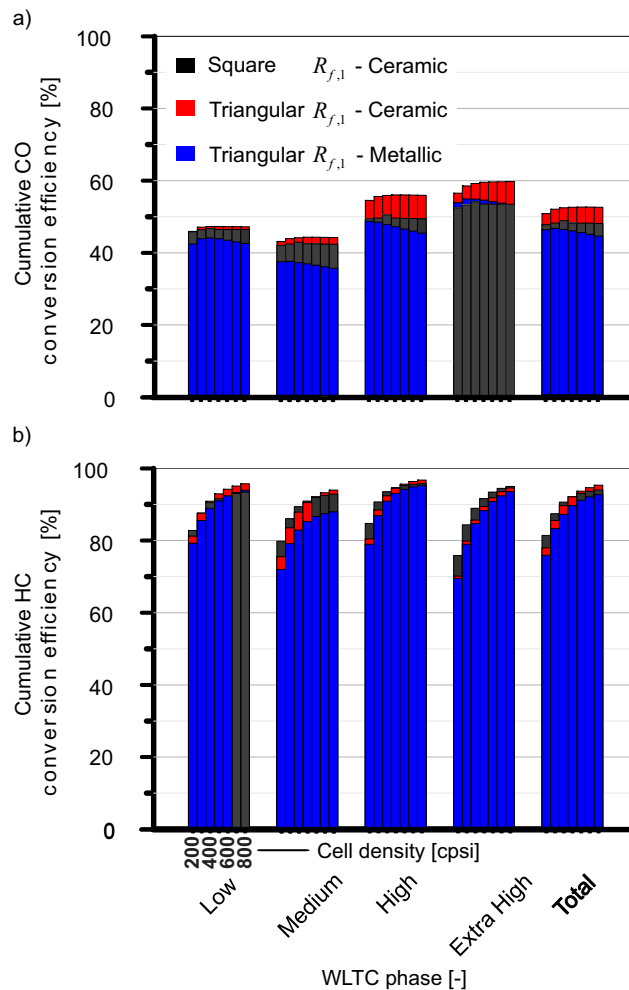
29

Figure 13: Cumulative conversion efficiency per WLTC phase for (a) CO and (b) HC as a function of the cell density with maximum fillet radius for square and triangular cells.

shows how the mass transfer coefficient and the internal pore diffusion efficiency reached higher values as the cell density moved towards its maximum value. The mass transfer coefficient is very sensitive, guided by the increase in monolith specific surface. By contrast, the internal pore diffusion efficiency also improves, but, as expected, shows the most relevant enhancement at an intermediate temperature range (medium velocity phase).

The changes in specific surfaces and mass transfer as the cell density is increased produce a gradual enhancement of the cumulative HC conversion efficiency, which showed an absolute variation between 15% and 20%. The alternation between triangular and square cells in ceramic
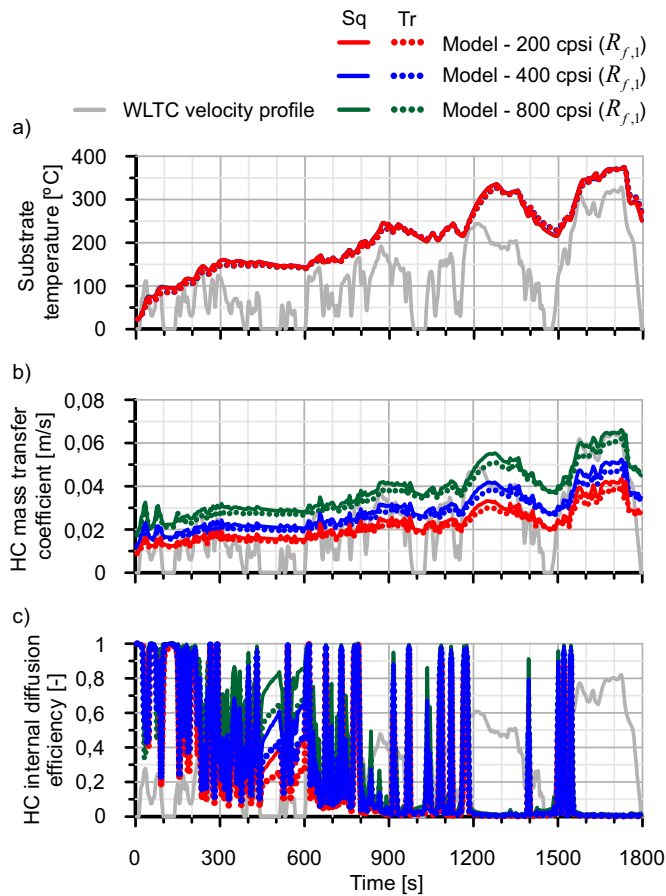
30

Figure 14: Comparison of the mass transfer parameters as a function of the cell density and shape: (a) Substrate temperature, (b) HC mass transfer coefficient and (c) HC internal pore diffusion efficiency.

monoliths as maximum efficiency solution obeys to the balance between phenomena affected in different degree as a function of the cell density. In particular, the specific surfaces favour the triangular cells, the mass transfer benefits the square cells and the substrate temperature varies slightly faster in square cells due to the lower radial conductivity and thermal capacitance. Although this last response is positive during periods of sustained acceleration, a penalty is obtained during deceleration processes. With respect to cumulative CO conversion efficiency, the WLTC phases did not show sensitivity to the cell density over 400 cpsi in ceramic monoliths. The improvement in mass transfer is not enough to deal with the high limitations related to sudden CO raw emission during accelerations. In fact, the triangular ceramic monolith provided the best per-

31

formance, phase after phase and especially in the higher temperature conditions. This is due to the synergistic effect of the higher gas specific surface and the lower washcoat specific surface in comparison to the square cells.

In all cases, the metallic monolith showed the worst performance. This low catalytic performance is mainly due to a slower warm up because of the higher thermal capacitance and radial conductivity. The latter, together with higher monolith specific surface as the cell density increases, makes the heat losses towards the environment play a relevant role. Hence, in combination with the mass transfer limitations, a decrease in cumulative CO conversion efficiency was found in each WLTC phase for the metallic substrate as the cell density was increased.

6. Conclusions

The influence of the cell geometry on the conversion efficiency of honeycomb catalytic converters was analysed under real driving conditions. A model with sensitivity to the flow properties and cell geometry in terms of mass and heat transfer was employed for this purpose. In particular, the effect of washcoat loading and cell density was analysed for ceramic and metallic monoliths with square and triangular cells taking as reference experimental data obtained from a commercial oxidation catalyst. The main findings of this work are:

- The increase of the washcoat loading favoured the catalyst conversion efficiency for all cell geometries, with higher impact on triangular cells. The increase of the gas specific surface and the decrease of the washcoat specific surface with an increase of the washcoat loading have been identified as the primary parameters controlling catalyst conversion efficiency. Other phenomena affected by the washcoat loading, such as thermal response, diffusion or residence time played a secondary role.

- Despite of the benefits of cell density increase on mass transfer, CO conversion found the optimum cell density at 400 cpsi for WLTC. The reason is a trade-off between increased mass transfer and gas specific surface with increased washcoat specific surface. Additionally, CO emission spikes were not able to be handled by cell geometry optimization.

32

- HC conversion was benefited by the cell density increase because of the higher conversion efficiency due to the HC adsorption mechanism at low temperature and HC higher sensitivity to mass transfer improvements than CO due to the lack of emission spikes as those affecting CO.

- The use of metallic substrates did not show an advantage in catalyst conversion efficiency when compared to the ceramic substrate under the studied boundaries. The lower catalyst conversion efficiency for metallic substrates is due to the increase of the heat transfer area and the higher radial conductivity leading to lower substrate temperature and longer warm-up periods compared to ceramic substrates.

Acknowledgements

References

[1] Gao, J., Chen, H., Li, Y., Chen, J., Zhang, Y., Dave, K., Huang, Y., 2019. Fuel consumption and exhaust emissions of diesel vehicles in worldwide harmonized light vehicles test cycles and their sensitivities to eco-driving factors. Energy Convers. Manag. 196, 605-613.

[2] Joshi, A., 2020. Review of vehicle engine efficiency and emissions, in: SAE Technical Paper 2020-01-0352.

[3] Theis, J., Getsoian, A., Lambert, C., 2018. The development of low temperature three-way catalysts for high efficiency gasoline engines of the future: Part II, in: SAE Technical Paper 2018-01-0939.

[4] Zuo, Q., Xie, Y., Guan, Q., Zhu, G., E, J., Zhu, X., Tang, Y., Wang, Z., Chen, W., 2020. Effect of critical dual-carrier structure parameters on performance enhancement of a dual-carrer catalytic converter and the gasoline engine system. Energy Convers. Manag. 204, 112325.

[5] Zhang, Q., Ren, X., Wu, X., Li, J., Chen, C., Wang, J., Sun, Y., Ji, H., Chen, S., 2018. Emission control system designing to meet China 6, in: SAE Technical Paper 2018-01-1706.

[6] Luján, J.M., Bermúdez, V., Dolz, V., Monsalve-Serrano, J., 2018. An assessment of the real-world driving gaseous emissions from a Euro 6 light-duty diesel vehicle using a portable emissions measurement system (PEMS), Atmos. Environ. 174, 112-121.

[7] García, A., Monsalve-Serrano, J., Villalta, D., Sari, R.L., 2019. Performance of a conventional diesel aftertreatment system used in a medium-duty multi-cylinder dual-mode dual-fuel engine. Energy Convers. Manag. 184, 327-337.

[8] Guilain, S., 2018. New challenges and key technologies of air system for future diesel and gasoline engines, in: Thiesel 2018, Conference on Thermo- and Fluid Dynamic Processes in Direct Injection Engines, Valencia, Spain.

[9] Fayad, M.A., Fernández-Rodríguez, D., Herreros, J.M., Lapuerta, M., Tsolakis, A., 2018. Interactions between aftertreatment systems architecture and combustion of oxygenated fuels for improved low temperature catalysts activity. Fuel 229, 189-197.

[10] Getsoian, A.B., Theis, J.R., Lambert, C.K., 2018. Sensitivity of three-way catalyst light-off temperature to air-fuel ratio. Emiss. Control Sci. Technol. 4 (3), 136-142.

[11] García, A., Piqueras, P., Monsalve-Serrano, J., Sari, R.L., 2018. Sizing a conventional diesel oxidation catalyst to be used for RCCI combustion under real driving conditions. Appl. Therm. Eng. 140, 62-72.

[12] Serrano, J.R., Climent, H., Piqueras, P., Angiolini, E., 2014. Analysis of fluid-dynamic guidelines in diesel particulate filter sizing for fuel consumption reduction in post-turbo and pre-turbo placement. Appl. Energy 132, 507-523.

[13] Serrano, J.R., Bermúdez, V., Piqueras, P., Angiolini, E., 2017. On the impact of DPF downsizing and cellular geometry on filtration efficiency in pre- and post-turbine placement. J. Aerosol Sci. 113, 20-35.

[14] Ramanathan, K., West, D.H., Balakotaiah, V., 2004. Optimal design of catalytic converters for minimizing cold-start emissions. Catal. Today 98 (3), 357-373.

[15] Novák, V., Dudák, M., Kočí, P., Marek, M., 2015. Understanding the gas transport in porous catalyst layers by using digital reconstruction techniques. Curr. Opin. Chem. Eng. 9, 16-26.

[16] Depcik, C.D., Hausmann, A.J., 2013. Review and a methodology to investigate the fffects of monolithic channel geometry. J. Eng. Gas Turbines Power 135 (3), 032301 1-16.

[17] Hughes, K.W., Flörchinger, P., 2002. Ultra thinwall light-off performance - Varying substrates, catalysts, and flow Rates; models and engine testing, in: SAE Technical Paper 2002-01-0352.

[18] Umehara, K., Yamada, T., Hijikata, T., Ichikawa, Y., Katsube, F., 1997. Advanced ceramic substrate: catalytic performance improvement by high geometric surface area and low heat capacity, in: SAE Technical Paper 971029.

[19] Cornejo, I., Nikrityuk, P., Hayes, R.E., 2020. The influence of channel geometry on the pressure drop in automotive catalytic converters: Model development and validation. Chem. Eng. Sci. 212, 115317.

[20] Heck, R.M., Robert, J.F., Gulati, S.T., 2009. Catalytic air pollution control. Commercial Technology. John Wiley & Sons.

[21] Santos, H., Costa, M., 2008. Evaluation of the conversion efficiency of ceramic and metallic three way catalytic converters. Energy Convers. Manag. 49, 291-300.

[22] Zhao, S., Zhang, J., Weng, D., Wu, X., 2003. A method to form well-adhered γ-Al2O3 layers on FeCrAl metallic supports. Surf. Coat. Technol. 167 (1), 97-105.

[23] Piqueras, P., García, A., Monsalve-Serrano, J., Ruiz, M.J., 2019. Performance of a diesel oxidation catalyst under diesel-gasoline reactivity controlled compression ignition combustion conditions. Energy Convers. Manag. 196, 18-31.

[24] Galindo, J., Serrano, J.R., Piqueras, P., García-Afonso, O., 2012. Heat transfer modelling in honeycomb wall-flow diesel particulate filters. Energy 43 (1), 201-213.

[25] Depcik, C., Assanis, D., 2005. One-dimensional automotive catalyst modeling. Prog. Energy Combust. Sci. 31 (4), 308-369.

[26] Kryl, D., Kočí, P., Kubíček, M., Marek, M., Maunula, T., Härkönen, M., 2005. Catalytic converters for automobile diesel engines with adsorption of hydrocarbons on zeolites. Ind. Eng. Chem. Res. 44 (25), 9524-9534.

[27] Hawthorn, R.D., 1974. Afterburner catalysts effects of heat and mass transfer between gas and catalyst Surface. AIChE J 70, 428-438.

[28] Oh, S.H., Cavendish, J.C., 1982. Transients of monolithic catalytic converters. Response to step changes in feedstream temperature as related to controlling automobile emissions. Ind. Eng. Chem. Prod. Res. Dev. 21 (1), 29-37.

[29] Kočí, P., Štěpánek, F., Kubíček, M., Marek, M., 2007. Modelling of micro/nano-scale concentration and temperature gradients in porous supported catalysts. Chem. Eng. Sci. 62 (18-22), 5380-5385.

[30] Joshi, S.Y., Harold, M.P., Balakotaiah, V., 2009. On the use of internal mass transfer coefficients in modeling of diffusion and reaction in catalytic monoliths. Chem. Eng. Sci. 64 (23), 4976-4991.

[31] Santos, H., Costa, M., 2009. Modelling transport phenomena and chemical reactions in automotive three-way catalytic converters. Chem. Eng. J. 148, 173183.

[32] Fogler, H.S., 2016. Elements of chemical reaction engineering, Prentice-Hall.

[33] Zygourakis, K., Aris, R., 1983. Multiple oxidation reactions and diffusion in the catalytic layer of monolith reactors. Chem. Eng. Sci. 38 (5), 733-744.

[34] Santos, H., Costa, M., 2008. The relative importance of external and internal transport phenomena in three way catalysts. Int. J. Heat Mass Transf. 51 (5-6), 1409-1422.

[35] Aris, R., 1975. The mathematical theory of diffusion and reaction in permeable catalysts, Vol. 1 Clarendon Press, Oxford.

[36] Payri, F., Arnau, F.J., Piqueras, P., Ruiz, M.J., 2018. Lumped approach for flow-through and wall-flow monolithic reactors modelling for real-time automotive applications, in: SAE Technical Paper 2018-01-0954.

563 [37] Zhang, F., Hayes, R.E., Kolaczkowski, S.T., 2004. A new technique to measure the effective diffusivity in a

564 catalytic monolith washcoat. Chem. Eng. Res. Des. 82 (4), 481-489.

565 [38] Cybulski, A., Moulijn, J.A., 1994. Modelling of heat transfer in metallic monoliths consisting of sinusoidal cells.

566 Chem. Eng. Sci. 49 (1), 19-27.

567 [39] Groppi, G., Tronconi, E., 1996. Continuous vs. discrete models of nonadiabatic monolith catalysts. AIChE J 42

568 (8), 2382-2387.

569 [40] Pukelsheim, F., 1994. The Three Sigma Rule. The American Statistician 48, 88-91.

570 [41] Gulati, S.T., 1988. Cell design for ceramic monoliths for catalytic converter application, in: SAE Technical

571 Paper 881685.

572 # Nomenclature

Acronyms

CAD	Crank angle degree
EGR	Exhaust gas recirculation
MIF	Mechanical integrity factor
OFA	Open frontal area
TIF	Thermal integrity factor
VGT	Variable geometry turbine
573 WLTC	World harmonized light vehicles test cycle

Latin letters

a_n	First-order solution constant of species n [−]
b_n	Zero-order solution constant of species n [−]
c_p	Specific heat [J/kgK]
C	Equivalent thermal capacitance [J/K]
D_h	Hydraulic diameter [m]
D_m	Molecular diffusivity [m^2/s]

36

E_a	Activation energy [J/mol]
G	Inhibition term [−]
h	Heat transfer coefficient [W/m^{2}K]
k_m	Mass transfer coefficient [m/s]
k_r	Kinetic constant of reaction r [−]
L_c	Characteristic length [m]
L_{mon}	Monolith length [m]
Nu	Nusselt number [−]
P_f	Pre-exponential factor [-]
Pr	Prandtl number [−]
$\dot{q}_r$	Reaction power [W]
R	Thermal resistance [K/W]
R_f	Fillet radius [m]
R_n	Reaction rate of species n [1/s]
Re	Reynolds number [−]
Sc	Schmidt number [−]
S	Cross-section area [m^2]
S_p	Specific surface [m^{-1}]
Sh	Sherwood number [−]
T	Temperature [K]
u	Velocity [m/s]
V	Volume [m^3]
w	Thickness [m]
x	Axial coordinate [m]
X	Mole fraction [−]

574

Greek letters

| α | Channel width [m] |

37

Δt	Time-step [s]
ε	Porosity [−]
η_{int}	Internal pore diffusion efficiency [−]
θ	Surface coverage [−]
Θ_{wc}	Washcoat fraction over the solid cross-section area [−]
κ	Conductivity [W/mK]
μ	Mean value [−]
ν	Stoichiometric coefficient [−]
ρ	Density [kg/m^3]
σ	Cell density [1/m^2]
σ_e	Standard deviation [−]
τ	Residence time [s]
ψ	Specific storage capacity [mol/m^3]

Subscripts

ads	Adsorption
ax	Axial
c	Conduction
cat	Catalyst
cell	Catalyst cell
des	Desorption
ext	External
gas	Exhaust gas flow
in	Inlet
int	Internal
mon	Monolith
n	Species
out	Outlet

ox	Oxidation
post	Downstream of the monolith
pre	Upstream of the monolith
r	Reaction
rad	Radial
sq	Square
sur	Surface
tr	Triangular
w	Substrate
wc	Washcoat

576